

Article

The Inclined Factors of Magnetic Field and Shrinking Sheet in Casson Fluid Flow, Heat and Mass Transfer

Shahanaz Parvin ¹, Siti Suzilliana Putri Mohamed Isa ^{1,2,*}, Norihan Md Arifin ^{1,3} and Fadzilah Md Ali ^{1,3}

¹ Institute for Mathematical Research, Universiti Putra Malaysia UPM, Serdang 43400, Selangor Darul Ehsan, Malaysia; spshoma@gmail.com (S.P.); norihana@upm.edu.my (N.M.A.); fadzilahma@upm.edu.my (F.M.A.)

² Centre of Foundation Studies for Agricultural Science, Universiti Putra Malaysia UPM, Serdang 43400, Selangor Darul Ehsan, Malaysia

³ Department of Mathematics, Universiti Putra Malaysia UPM, Serdang 43400, Selangor Darul Ehsan, Malaysia

* Correspondence: ctsuzilliana@upm.edu.my

Abstract: The development of the mathematical modeling of Casson fluid flow and heat and mass transfer is presented in this paper. The model is subjected to the following physical parameters: shrinking parameter, mixed convection, concentration buoyancy ratio parameter, Soret number, and Dufour number. This model is also subjected to the inclined magnetic field and shrinking sheet at a certain angle projected from the y - and x -axes, respectively. The MATLAB bvp4c program is the main mathematical program that was used to obtain the final numerical solutions for the reduced ordinary differential equations (ODEs). These ODEs originate from the governing partial differential equations (PDEs), where the transformation can be achieved by applying similarity transformations. The MATLAB bvp4c program was also implemented to develop stability analysis, where this calculation was executed to recognize the most stable numerical solution. Numerical graphics were made for the skin friction coefficient, local Nusselt number, local Sherwood number, velocity profile, temperature profile, and concentration profile for certain values of the physical parameters. It is found that all the governed parameters affected the variations of the Casson fluid flow, heat transfer, mass transfer, and the profiles of velocity, temperature, and concentration. In addition, a stable solution can be applied to predict the impact of physical parameters on the actual fluid model by using a mathematical fluid model.

Keywords: mathematical modeling; double-diffusive; casson fluid; exponentially shrinking; stability analysis; MATLAB bvp4c



Citation: Parvin, S.; Mohamed Isa, S.S.P.; Arifin, N.M.; Md Ali, F. The Inclined Factors of Magnetic Field and Shrinking Sheet in Casson Fluid Flow, Heat and Mass Transfer. *Symmetry* **2021**, *13*, 373. <https://doi.org/10.3390/sym13030373>

Academic Editors: Sergei D. Odintsov and Marek Szafranski

Received: 25 January 2021

Accepted: 20 February 2021

Published: 25 February 2021

Publisher's Note: MDPI stays neutral with regard to jurisdictional claims in published maps and institutional affiliations.



Copyright: © 2021 by the authors. Licensee MDPI, Basel, Switzerland. This article is an open access article distributed under the terms and conditions of the Creative Commons Attribution (CC BY) license (<https://creativecommons.org/licenses/by/4.0/>).

1. Introduction

Double-diffusive convection, or double diffusion, is a type of convection in which the process of transferring heat is induced by the concentration and temperature difference that occurs within the involved physical systems. The two components (concentration or temperature gradients) are under the controlling factor of gravitational acceleration, and they have various rates of diffusion. Double diffusion occurs naturally in lakes, oceans, solar ponds, and the atmosphere. Furthermore, this type of convection exists in industrial applications such as crystal growth, chemical manufacturing, energy storage, and food processing. Pioneering reports of the fundamental concept in double-diffusive convection have been introduced, especially in natural convection [1–5]. Turner [1] presented a theoretical report on double diffusion, discussing the aspects of fluid layers and interfaces. Schmitt [2] summarized the application of double-diffusive convection in an ocean (namely oceanography), especially for a salt finger. The production of crystal from cooled magma due to double-diffusive convection is described in detail by Huppert and Sparks [3]. Ostrach [4] described the main role of the driving force in convection fluid flow, i.e., gravitational force. A comparison between theoretical and experimental reports on fundamental double-diffusive convection was made by Viskanta et al. [5], and related

phenomena regarding this type of convection are also discussed. Non-Newtonian fluid is a fluid with different characteristics in any way from those of Newtonian fluids. These fluids demonstrate either shear thickening or shear thinning. Shear thinning occurs when the viscosity of the fluid reduces as the shear rate enhances. On the contrary, shear thickening occurs when the viscosity of the fluid increases due to the decrement in the shear rate. One model of non-Newtonian fluid is Casson fluid, where a model of blood flow through narrow arteries demonstrates Casson fluid behaviors.

There are pioneering works regarding double-diffusive Newtonian fluid convection. Magnetohydrodynamic double-diffusive mixed convection in a Newtonian fluid, passing through a linear stretching surface in a porous medium of the Darcian model, was considered by Bég et al. [6]. Double-diffusive mixed convection Newtonian fluid from an exponential function of a stretching surface by applying a numerical technique, namely the Keller box method, was explored by Srinivasacharya and RamReddy [7]. Subsequently, the problem by Srinivasacharya and RamReddy [7] was extended by Sreenivasulu and Bhaskar Reddy [8] by adding the effects of viscous dissipation and thermal radiation. A numerical study of Newtonian fluid flow induced by an exponential permeable stretching sheet, designed in a three-dimensional model, was presented by Hayat et al. [9]. Their mathematical model included the impacts of a heat source/sink and a chemical reaction. Isa et al. [10] developed a stability analysis of dual-numerical solutions, reporting the case of double-diffusive mixed convection Newtonian fluid flow bounded by an exponentially shrinking sheet in the presence of the following parameters: Soret, Dufour, mixed convection, the buoyancy ratio, and shrinking. Hazirah et al. [11] reported the numerical findings of heat and mass transmission together with the features of Newtonian fluid flow, where the fluid is bounded by an inclined stretching/shrinking sheet. Roşca et al. [12] selected the most stable and physically relevant in actual fluid among the dual-numerical solution for the double-diffusive convection of a Newtonian fluid. The solutions they produced were under the condition of when the sheet was stretched or shrieked linearly. They also applied the Lie group symmetry technique to obtain the ordinary differential equations (ODEs). The similarity between the techniques of Srinivasacharya and RamReddy [7], Sreenivasulu and Bhaskar Reddy [8], Hayat et al. [9], Isa et al. [10], and Hazirah et al. [11] are as follows: they used the appropriate term, which is $\exp(x/2L)$, in the boundary conditions for the parts of the concentration and temperature distributions. As a result, the final numerical findings fulfill the fixed boundary conditions, and this term is accepted to proceed with the subsequent calculations.

The latest reports on double-diffusive convection in Casson fluid have been published. The characteristics of double-diffusive mixed convection with the limitations of a chemical reaction, thermal radiation, the Soret and Dufour parameters, and exponential variation of the stretching surface were studied by Sharada and Shankar [13]. The description of double-diffusive three-dimensional magnetohydrodynamics radiating Casson fluid was reported by Gireesha et al. [14], who used a numerical method, namely the Runge–Kutta–Fehlberg fourth-fifth-order (RKF45) method. The report provided by Gireesha et al. [14] considers the restrictions when the fluid is bounded by convective conditions and when the sheet beyond the fluid is stretched linearly. Kumar et al. [15] performed a numerical finding (RKF45) to obtain results on the double-diffusive mixed convection of Casson fluid induced by a sheet stretched in a nonlinear function. The steady magnetohydrodynamics double-diffusive Casson fluid beyond a permeable surface was explored by Pal and Roy [16]. The surface they used was stretched or shrieked by a nonlinear variation. They also included the effects of a chemical reaction, viscous dissipation, Ohmic dissipation, thermophoresis, and Brownian motion. The unsteady state of mixed convection in Casson fluid due to a stretched linear sheet was reported by Ullah et al. [17]. They set up boundaries with the conditions at the boundary, namely slip and convective effects. Das et al. [18] described the effects of the Soret–Dufour parameter, slip parameter, unsteadiness parameter, porosity parameter, and a chemical reaction on an unsteady magnetohydrodynamics Casson fluid. Prasad et al. [19] applied the finite-element method to analyze the unsteady state of Casson

fluid flow bounded by an accelerated vertical wavy plate. The system [19] was governed by an inclination angle, chemical reaction, heat generation, and thermal radiation. Triple-diffusive Casson fluid convection along a horizontal plate saturated with two various salts, which form three components of diffusion, were solved numerically by Archana et al. [20]. These components are temperature gradient, concentration gradient for the first salt, and concentration gradient for the second salt. The stagnation point of Casson fluid flow over a cylinder-covered catalyst layer was studied by Alizadeh et al. [21], subjected to the effect of the Soret–Dufour parameter and chemical species transfer. Casson nanofluid flow over a nonlinear inclined stretching sheet was studied by Rafique et al. [22] with the impacts of convective boundaries, thermal radiations, Brownian motion, and thermophoresis diffusion. Recently, Lund et al. [23,24] produced multiple numerical solutions on the mathematical model of Casson fluid by taking into account the additional factors: (1) Stefan blowing and slip conditions [23] and (2) convective condition and stagnation flow [24].

The convection induced by the transmission of two components simultaneously, mass and heat, are known as Soret and Dufour effects, respectively. The temperature difference induces mass transfer (Soret effect), and the concentration difference generates heat transfer (Dufour effect). From experimental reports, the diffusion components (heat and particles) become beneficial when these two gradients are very large. Finally, the Soret and Dufour impacts play a significant role in this type of convection. The boundary layer fluid flow with the Soret–Dufour parameters has significant contributions to heat insulation, compact heat exchangers, paper production, drying technology, and catalytic reactors [25]. The impacts of the Soret–Dufour parameter in double-diffusive mixed convection Newtonian fluid [6–11] and Casson fluid [13–15,17–21] were published. Furthermore, the study of Soret–Dufour effects on other types of fluids or for the various forms have been reported. Khan and Sultan [26] studied Eyring–Powell fluid in a cone by researching the aspects of double-diffusive convection with Soret–Dufour impacts. They implemented the optimal homotopy analysis method (OHAM) in their problem. The impact of the Soret–Dufour parameters on double-diffusive mixed convection in a lid-driven cavity was explained by Kefayati [27], who used Newtonian and shear-thinning fluids. They used the finite-difference lattice Boltzmann method (FDLBM) to deal with their numerical problem. The analytical and numerical solutions to double-diffusive convection in a binary fluid were obtained by Lagra et al. [28], with the presence of the Soret and Dufour parameters. The comparison among analytical and numerical solutions in this problem [28] showed good agreement. Kasmani et al. [29] inspected the presence of Soret–Dufour effects and thermal radiation on the double-diffusive flow of nanofluid submerged in a permeable wedge. Their governing equations were solved by the fourth-order Runge–Kutta–Gill method combined with the shooting and Newton–Raphson methods.

The literature review shows that the stability analysis of the double-diffusive Casson fluid flow bounded by an exponential function of the shrinking sheet, but the inclination angles at the magnetic field and shrinking sheet are not yet reported. Previous reports of stability analysis on numerical results related to boundary layer fluid flow and heat and mass transfer can be found by the following papers: (1) Casson fluid [23,24] and (2) nanofluid [30–32]. The effects of the mixed convection parameter, concentration buoyancy ratio parameter, Soret–Dufour parameters, and shrinking parameter are discussed in detail. These parameters impact the increment or decrement in the related profiles (velocity, temperature, and concentration) and physical parameters (skin friction coefficient, local Nusselt number, and local Sherwood number). In Section 2 of this paper, the mathematical formulation is presented. The Results and Discussion are presented in Section 3. A conclusion is presented in the final section, which is Section 4.

2. Methodology

2.1. Problem Formulation

The two-dimensional Cartesian model of electrically conducting viscous and incompressible Casson fluid is considered, and this model is bounded by an exponential function

of the shrinking sheet with velocity u_w . The gravitational acceleration g is applied perpendicularly to the reference horizontal axis, and the shrinking sheet is projected by a certain angle ϵ from the same reference axis [11]. The shrinking vector is directed to the center of the sheet. Furthermore, the constant applied magnetic field B_0 is inclined by the inclination angle δ from the y -axis [33]. The components of velocity in the x - and y -directions are denoted by u and v , respectively. The temperature and the concentration at the plane are, namely, T_w and C_w , and the temperature and the concentration at the inviscid fluid are labeled as T_∞ and C_∞ , respectively. Wall mass suction velocity is presented as $v_w(x) > 0$. The two-dimensional Cartesian model for the current problem is depicted in Figure 1. The related governing equations are stated as below:

$$\frac{\partial u}{\partial x} + \frac{\partial v}{\partial y} = 0, \tag{1}$$

$$u \frac{\partial u}{\partial x} + v \frac{\partial u}{\partial y} = v \left(1 + \frac{1}{\omega} \right) \frac{\partial^2 u}{\partial y^2} + g\beta_T(T - T_\infty) \cos(\epsilon) + g\beta_C(C - C_\infty) \cos(\epsilon) + \frac{\sigma B_0^2}{\rho} \sin^2(\delta) u, \tag{2}$$

$$u \frac{\partial T}{\partial x} + v \frac{\partial T}{\partial y} = \alpha \frac{\partial^2 T}{\partial y^2} + \frac{DK_T}{C_s C_p} \frac{\partial^2 C}{\partial y^2}, \tag{3}$$

$$u \frac{\partial C}{\partial x} + v \frac{\partial C}{\partial y} = D \frac{\partial^2 C}{\partial y^2} + \frac{DK_T}{T_m} \frac{\partial^2 T}{\partial y^2}, \tag{4}$$

where $\nu = \mu/\rho$ is the kinematic viscosity, μ is the viscosity, ρ is the fluid density, ω is the Casson parameter, β_T is the coefficient of thermal expansion, β_C is the coefficient of solutal expansions, B_0 is the constant strength of the magnetic field, T is the temperature of the fluid, C is the concentration of the fluid, α is the thermal diffusivity, D is the solutal diffusivity of the medium, K_T is the thermal diffusion ratio, C_s is the concentration susceptibility, C_p is the specific heat at constant pressure, and T_m is the mean fluid temperature.

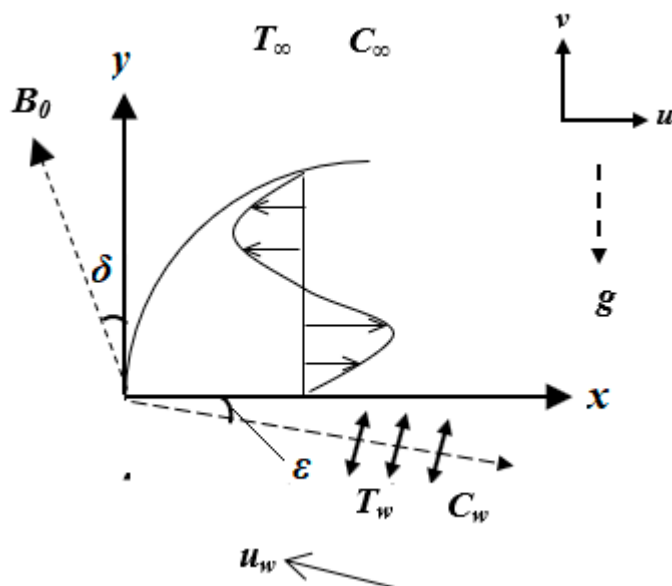


Figure 1. Schematic diagram of the model problem.

The appropriate boundary conditions are

$$\begin{aligned} u &= u_w(x) = \lambda U_0 \exp(x/L), \quad v = v_w(x), \\ T_w(x) &= T_\infty + T_0 \exp(x/2L), \quad C_w(x) = C_\infty + C_0 \exp(x/2L), \quad \text{at } y = 0, \\ u &\rightarrow 0, \quad T \rightarrow T_\infty, \quad C \rightarrow C_\infty \quad \text{as } y \rightarrow \infty, \end{aligned} \tag{5}$$

where $\lambda < 0$ is the shrinking parameter, and L is the length of the sheet. The term $\exp(x/2L)$ in temperature T_w and concentration C_w has been used by previous investigators [7–11], which are appropriate for our mathematical model, two-dimensional fluid flow, which is subjected to the Sore–Dufour parameters.

The physical parameters of the skin friction coefficient C_f , local Nusselt number Nu_x , and local Sherwood number Sh_x are presented as follows:

$$C_f = \left(\frac{\mu}{\rho U_0^2} \right) \left(\frac{\partial u}{\partial y} \right), \quad Nu_x = \left(\frac{L}{T_w - T_\infty} \right) \left(-\frac{\partial T}{\partial y} \right)_{y=0}, \quad Sh_x = \left(\frac{L}{C_w - C_\infty} \right) \left(-\frac{\partial C}{\partial y} \right)_{y=0}, \quad (6)$$

Introducing new similarity variables:

$$\theta(\eta) = \frac{T-T_\infty}{T_w-T_\infty}, \quad \varphi(\eta) = \frac{C-C_\infty}{C_w-C_\infty}, \quad \eta = y \left(\frac{U_0}{2vL} \right)^{1/2} \exp(x/2L), \quad (7)$$

$$u = U_0 \exp(x/L) f'(\eta), \quad v = - \left(\frac{vU_0}{2L} \right)^{1/2} \exp(x/2L) [f(\eta) + \eta f'(\eta)],$$

where η is a boundary layer thickness for the fluid model. The similarity variables u and v are obtained by performing $u = \partial\psi/\partial y$ and $v = -\partial\psi/\partial x$, where ψ is the stream function for exponential velocity at the sheet. This stream function is stated as

$$\psi(x, y) = (2vLU_0)^{1/2} \exp(x/2L) f(\eta) \quad (8)$$

2.2. Method of Solution

Equation (7) is substituted into (2)–(6), and the following equations are obtained:

$$\left(1 + \frac{1}{\omega} \right) f''' + ff'' - 2(f')^2 + 2Ri(\theta + N\varphi) \cos \varepsilon - 2H \sin^2(\delta) f' = 0, \quad (9)$$

$$\frac{1}{Pr} \theta'' + f\theta' - f'\theta + Db\varphi'' = 0, \quad (10)$$

$$\frac{1}{Sc} \varphi'' + f\varphi' - f'\varphi + Sr\theta'' = 0, \quad (11)$$

$$f'(\eta) = \lambda, \quad f(\eta) = S, \quad \theta(\eta) = 1, \quad \varphi(\eta) = 1 \quad \text{at } \eta = 0, \quad (12)$$

$$f'(\eta) \rightarrow 0, \quad \theta(\eta) \rightarrow 0, \quad \varphi(\eta) \rightarrow 0 \quad \text{as } \eta \rightarrow \infty,$$

$$C_f \frac{\sqrt{Re_x}}{2} \exp\left(\frac{-3X}{2}\right) = f''(0), \quad Nu_x \sqrt{\frac{2}{Re_x}} \exp\left(\frac{-X}{2}\right) = -\theta'(0), \quad (13)$$

$$Sh_x \sqrt{\frac{2}{Re_x}} \exp\left(\frac{-X}{2}\right) = -\varphi'(0).$$

The parameters involved in this problem are the mixed convection parameter $Ri = Gr/Re^2$, magnetic field parameter $H = \sigma LB_0^2 e^{-x/L}/\rho U_0$, thermal Grashof number $Gr = g\beta_T(T_0 - T_\infty)L^3 e^{x/2L}/v^2$, Reynolds number $Re = u_0 L e^{x/L}/v$, concentration buoyancy ratio $N = \beta_C(C_0 - C_\infty)/\beta_T(T_0 - T_\infty)$, Prandtl number $Pr = v/\alpha$, Schmidt number $Sc = v/D$, Soret number $Sr = DK_T(T_0 - T_\infty)/T_m v(C_0 - C_\infty)$, Dufour number $Db = DK_T(C_0 - C_\infty)/C_s C_p v(T_0 - T_\infty)$, and suction parameter S . The parameter S is defined as $S = (v_w(x)/\exp(x/2L)) \times \sqrt{2L/vU_0} > 0$. Positive Ri indicates the case of aiding flow, negative Ri for opposing flow, and zero Ri for forced convection flow. Moreover, N can be positive and negative values together with $N = 0$ (in the absence of mass transfer).

2.3. Stability Analysis

The unsteady state of governing Equations (2)–(4) is introduced as below, where t is time. This is a first step for stability analysis: to select a stable and physically reliable solution.

$$\frac{\partial u}{\partial t} + u \frac{\partial u}{\partial x} + v \frac{\partial u}{\partial y} = v \left(1 + \frac{1}{\omega} \right) \frac{\partial^2 u}{\partial y^2} + g\beta_T(T - T_\infty) \cos(\varepsilon) + g\beta_C(C - C_\infty) \cos(\varepsilon) + \frac{\sigma B_0^2}{\rho} \sin^2(\delta) u, \quad (14)$$

$$\frac{\partial T}{\partial t} + u \frac{\partial T}{\partial x} + v \frac{\partial T}{\partial y} = \alpha \frac{\partial^2 T}{\partial y^2} + \frac{DK_T}{C_s C_p} \frac{\partial^2 C}{\partial y^2}, \quad (15)$$

$$\frac{\partial C}{\partial t} + u \frac{\partial C}{\partial x} + v \frac{\partial C}{\partial y} = D \frac{\partial^2 C}{\partial y^2} + \frac{DK_T}{T_m} \frac{\partial^2 T}{\partial y^2}, \quad (16)$$

The boundary conditions and similarity variables in unsteady state are shown as

$$\begin{aligned} \frac{\partial f}{\partial \eta}(\eta, \tau) = \lambda, \quad f(\eta, \tau) = S, \quad \theta(\eta, \tau) = 1, \quad \varphi(\eta, \tau) = 1 \quad \text{at } \eta = 0, \\ \frac{\partial f}{\partial \eta}(\eta, \tau) \rightarrow 0, \quad \theta(\eta, \tau) \rightarrow 0, \quad \varphi(\eta, \tau) \rightarrow 0 \quad \text{as } \eta \rightarrow \infty, \end{aligned} \quad (17)$$

$$\begin{aligned} \theta(\eta, \tau) = \frac{T - T_\infty}{T_w - T_\infty}, \quad \varphi(\eta, \tau) = \frac{C - C_\infty}{C_w - C_\infty}, \\ \tau = \frac{U_0}{2L} (\exp(x/L)) t, \quad \eta = y \left(\frac{U_0}{2vL} \right)^{1/2} \exp(x/2L), \\ u = U_0 \exp(x/L) \frac{\partial}{\partial \eta} f(\eta, \tau), \\ v = -\frac{\eta}{2L} \sqrt{2vLU_0} \exp(x/2L) \frac{\partial}{\partial \eta} f(\eta, \tau) \\ - \frac{U_0}{2L^2} \exp(3x/L) t \sqrt{2vLU_0} \frac{\partial}{\partial \tau} f(\eta, \tau) \\ - \frac{1}{2L} \sqrt{2vLU_0} \exp(x/2L) f(\eta, \tau). \end{aligned} \quad (18)$$

From Equation (18), the dimensionless time variable τ for exponential velocity at the sheet is presented by $\tau = (U_0/2L) [\exp(x/L)] t$. In the stability analysis section, the variable τ is used for all the calculations, and τ is observed to depend on t [34].

The equations introduced by previous investigators [34] for stability analysis are stated as follows:

$$\begin{aligned} f(\eta, \tau) = f_0(\eta) + (\exp(-\gamma\tau)) F(\eta, \tau), \\ \theta(\eta, \tau) = \theta_0(\eta) + (\exp(-\gamma\tau)) G(\eta, \tau), \\ \varphi(\eta, \tau) = \varphi_0(\eta) + (\exp(-\gamma\tau)) J(\eta, \tau), \end{aligned} \quad (19)$$

where γ denotes an unknown eigenvalue, and $F(\eta, \tau)$, $G(\eta, \tau)$, and $J(\eta, \tau)$ are small relative to $f_0(\eta)$, $\theta_0(\eta)$, and $\varphi_0(\eta)$.

2.4. Method of Solution for Stability Analysis

First, substitute Equation (18) in Equations (14)–(16) to obtain the equations below:

$$\begin{aligned} \left(1 + \frac{1}{\omega}\right) \frac{\partial^3 f}{\partial \eta^3} + f \frac{\partial^2 f}{\partial \eta^2} - 2 \left(\frac{\partial f}{\partial \eta}\right)^2 + 2Ri \cos(\varepsilon) \theta + 2Ri N \cos(\varepsilon) \varphi \\ - \frac{\partial^2 f}{\partial \eta \partial \tau} + 2\tau \frac{\partial f}{\partial \tau} \frac{\partial^2 f}{\partial \eta^2} - 2\tau \frac{\partial f}{\partial \eta} \frac{\partial^2 f}{\partial \eta \partial \tau} - 2H \sin^2(\delta) \frac{\partial f}{\partial \eta} = 0, \end{aligned} \quad (20)$$

$$\frac{1}{Pr} \frac{\partial^2 \theta}{\partial \eta^2} + f \frac{\partial \theta}{\partial \eta} - \frac{\partial f}{\partial \eta} \theta + Db \frac{\partial^2 \varphi}{\partial \eta^2} - \frac{\partial \theta}{\partial \tau} - 2\tau \frac{\partial \theta}{\partial \tau} \frac{\partial f}{\partial \eta} + 2\tau \frac{\partial f}{\partial \tau} \frac{\partial \theta}{\partial \eta} = 0. \quad (21)$$

$$\frac{1}{Sc} \frac{\partial^2 \varphi}{\partial \eta^2} + f \frac{\partial \varphi}{\partial \eta} - \frac{\partial f}{\partial \eta} \varphi + Sr \frac{\partial^2 \theta}{\partial \eta^2} - \frac{\partial \varphi}{\partial \tau} - 2\tau \frac{\partial \varphi}{\partial \tau} \frac{\partial f}{\partial \eta} + 2\tau \frac{\partial f}{\partial \tau} \frac{\partial \varphi}{\partial \eta} = 0. \quad (22)$$

Next, substitute Equation (19) into Equations (20)–(22), and set $\tau = 0$. As a result, the following equations are obtained:

$$\begin{aligned} \left(1 + \frac{1}{\omega}\right) F_0''' + f_0 F_0'' + f_0' F_0 - 4f_0' F_0' + 2Ri \cos(\varepsilon) (G_0 + N J_0) \\ + [\gamma - 2H \sin^2(\delta)] F_0' = 0, \end{aligned} \quad (23)$$

$$\frac{1}{Pr} G_0'' + f_0 G_0' + \theta_0' F_0 - \theta_0 F_0' - G_0 f_0' + Db J_0'' + \gamma G_0 = 0, \quad (24)$$

$$\frac{1}{Sc} J_0'' + f_0 J_0' + \varphi_0' J_0 - \varphi_0 J_0' - J_0 f_0' + Sr G_0'' + \gamma J_0 = 0, \quad (25)$$

along with the boundary conditions:

$$\begin{aligned}
 F_0'(\eta) = 0, F_0(\eta) = 0, G_0(\eta) = 0, J_0(\eta) = 0 \text{ at } \eta = 0. \\
 F_0'(\eta) \rightarrow 0, G_0(\eta) \rightarrow 0, J_0(\eta) \rightarrow 0 \text{ as } \eta \rightarrow \infty.
 \end{aligned}
 \tag{26}$$

By relaxing any one of the boundary conditions in $\eta \rightarrow \infty$, eigenvalues will be obtained [35]. In this paper, the boundary condition $F_0'(\infty) \rightarrow 0$ is relaxed to become $F_0''(0) = 1$. Finally, Equations (23)–(26) with the new relaxing boundary condition are solved in MATLAB.

3. Results and Discussion

Numerical graphics are depicted for the skin friction coefficient $C_f \sqrt{2\text{Re}_x} \exp(-3X/2)$, local Nusselt number $Nu_x(2/\text{Re}_x)^{1/2} \exp(-X/2)$, local Sherwood number $Sh_x(2/\text{Re}_x)^{1/2} \exp(-X/2)$, velocity profile $f'(\eta)$, temperature profile $\theta(\eta)$, and concentration profile $\varphi(\eta)$ for the following physical parameters: shrinking parameter λ , mixed convection Ri , concentration buoyancy ratio parameter N , Soret number Sr , and Dufour number Db . The numerical solutions obtained from this article are dual. They are labeled by the first solution (solid line) and the second solution (dashed line). In this paper, the following values are fixed for the entire MATLAB program, unless mentioned otherwise: $\omega = 2000$, $S = 2.5$, $\lambda = -0.4$, $\varepsilon = 50^\circ$, $\delta = 80^\circ$, $N = 1.0585$, $Ri = -0.0212$, $Sc = 0.5$, $Pr = 1$, $H = 0.4946$, $Db = 0.1002$, and $Sr = 1.8004$. Moreover, the largest of fluid thickness $\eta = 10$ is constantly used for numerical computations.

3.1. Verification of Numerical Accuracy

The validation of our numerical results obtained from MATLAB bvp4c is performed by presenting a comparison with the pioneering investigators in the case of the exponentially stretching sheet [30] and shrinking sheet. The stretching parameter is denoted by $\lambda > 0$, and the shrinking parameter is presented by $\lambda < 0$. This comparison is reported for the wall temperature gradient $-\theta'(0)$ values, as shown in Table 1. The formulation of the wall temperature gradient has been derived by a previous investigator [7]. As a result, the final formulation is obtained: $Nu_x/\sqrt{\text{Re}_x} = -\sqrt{X/2} \theta'(0)$. Those values show good agreement with the numerical data reported by Magyari and Keller [36] and Srinivasacharya and RamReddy [7].

Table 1. Comparison between the wall temperature gradient $\theta'(0)$ for $\omega = 1,000,000$, $Pr = 1$, and $H = Ri = Sc = Sr = Db = N = \delta = \varepsilon = 0$.

| S | λ | Magyari and Keller [36] | Srinivasacharya and RamReddy [7] | Present |
|---|-----------|-------------------------|----------------------------------|----------|
| 0 | 1.69550 | — | — | −0.77398 |
| | 1 | −0.59434 | −0.59438 | −0.59466 |
| | 0.97609 | — | — | −0.58804 |
| 2 | 0.06350 | — | — | −1.02075 |
| | −0.5 | — | — | −0.79220 |
| | −0.77869 | — | — | −0.49097 |

The verification of the MATLAB bvp4c program used in this paper was made by making an observation for all the profiles: velocity, temperature, and concentration. Both solutions showed that the instantaneous points at $\eta = 0$ and $\eta \rightarrow \infty$ fully satisfy the desired boundary conditions (Equation (11)). Therefore, this observation assures the accuracy of the applied numerical method.

3.2. Selection of a Physically Reliable Solution

Although the numerical solutions obtained in this paper are dual, we still have to choose a solution that is stable and physically reliable. Therefore, the most stable solution

can be chosen by using a numerical calculation, namely stability analysis. The results that occurred from the stable solution are predicted to exist in the actual state in fluid, which can be seen in the variation of profiles and physical parameters. Stability analysis was performed by calculating the smallest eigenvalues γ , as shown in Table 2. Positive values of γ indicate that there is an initial decay of disturbance, whereas the negative values of γ denote an initial growth of disturbance. The positive values denote that the solution is stable, and it is labeled as the first solution in the MATLAB program. Furthermore, negative eigenvalues represent the second solution. The second solution is assumed to be unstable and not physically occur in the actual fluid state.

Table 2. The smallest eigenvalues for different values of the mixed convection and buoyancy ratio parameters when $S = 1.685$.

| Ri | N | Solutions | |
|----------|-------|----------------|-----------------|
| | | First Solution | Second Solution |
| −0.01 | 0.500 | 0.08814 | −0.08963 |
| | 0.501 | 0.08498 | −0.08636 |
| | 0.502 | 0.08170 | −0.08297 |
| −0.01002 | 0.500 | 0.08394 | −0.08529 |
| | 0.501 | 0.08060 | −0.08185 |
| | 0.502 | 0.07712 | −0.07826 |

3.3. Variation in the Profiles of Velocity, Temperature, and Concentration

The profiles due to the control parameters λ , Ri , and N , are visualized in Figures 2–4, respectively. These profiles are plotted against the distance from the shrinking sheet η . These profiles show the satisfaction of boundary conditions (Equation (4)) at the points $\eta = 0$ and $\eta \rightarrow \infty$. The negative vector in velocity acts in an opposite direction to the reference positive stretching vector, as the sheet reported in this paper is compressed and influences the fluid flow and the rate of heat transfer and mass. However, the description of the velocity profile in this paper focuses on the values of velocity. The first solution shows the uniform decrement in the velocity magnitude due to the distance from the shrinking sheet η , until the velocity reaches a constant zero value. Therefore, the zero velocity at the point far from the shrinking sheet denotes there is no fluid movement at this point. The magnitude of velocity for the second solution increases for small η and reaches the maximum point. The maximum velocity for the second solution is denoted by the lowest minimum peak at the velocity profile. Then, the instantaneous velocity of the second solution decreases until it achieves a zero value. Moreover, all the temperature graphs show a continuous decrement in the instantaneous temperature for various fluid thickness η . The graphical representations of concentration show the existence of a maximum peak at small η . The concentration reaches a certain maximum point, and then it continuously reduces, and finally the concentration vanishes. As a conclusion, the MATLAB program declares the uniform variation in these profiles as the first solution, otherwise it is labeled as the second one. Uniform variation is described as a continuous increment or decrement, with the minimum existence of a peak.

The velocity in Figure 2 is found to decline with the increasing shrinking parameter $|\lambda|$, and other profiles increase due to the same parameter. This result is shown by the first solution. However, an opposite nature is visualized in the second solution in Figure 2. The distribution pattern of the velocity profile, which is influenced by the magnitude of the shrinking parameter, was published by previous investigators [37–39]. They proved that the reduction of instantaneous velocity is affected by the shrinking rate at the sheet. As a conclusion, the higher shrinking parameter increases the compressing rate at the fluid and causes the fluid velocity to slow down. Besides, Figure 2 also shows that the concentration and temperature of Casson fluid are enhanced for higher estimation of

$|\lambda|$ [31,32]. However, these reports [31,32] used the rate of the stretching/shrinking sheet λ , instead of the magnitude $|\lambda|$.

The first solution in Figure 3 demonstrates that the higher rate of the mixed convection parameter Ri (lower magnitude in the opposing flow rate) contributes to an increment in the Casson fluid velocity. Furthermore, the first solution in the profiles of temperature and concentration becomes smaller when the opposing flow magnitude decreases. These three profiles in the second solution show a reverse pattern due to the impact of the enhancing mixed convection parameter. As a conclusion, it is clear from Figure 3 that the velocity distribution is increased for the increment of Ri . This is because the addition of Ri enhances the buoyancy ratio, and fluid flow is accelerated. Therefore, the instantaneous velocity increases. Temperature and concentration decrease with increasing values of Ri . When the parameter Ri increases, it contributes to the increment of the convection cooling effect. As a result, the temperature and concentration reduce. On the other hand, the first solution pattern in Figure 4 illustrates that N reduces the variation of Casson velocity, while there is an increment in temperature and concentration profiles. Furthermore, an opposite pattern can be seen in the case of effect N on the profiles of velocity, temperature, and concentration in the second solution.

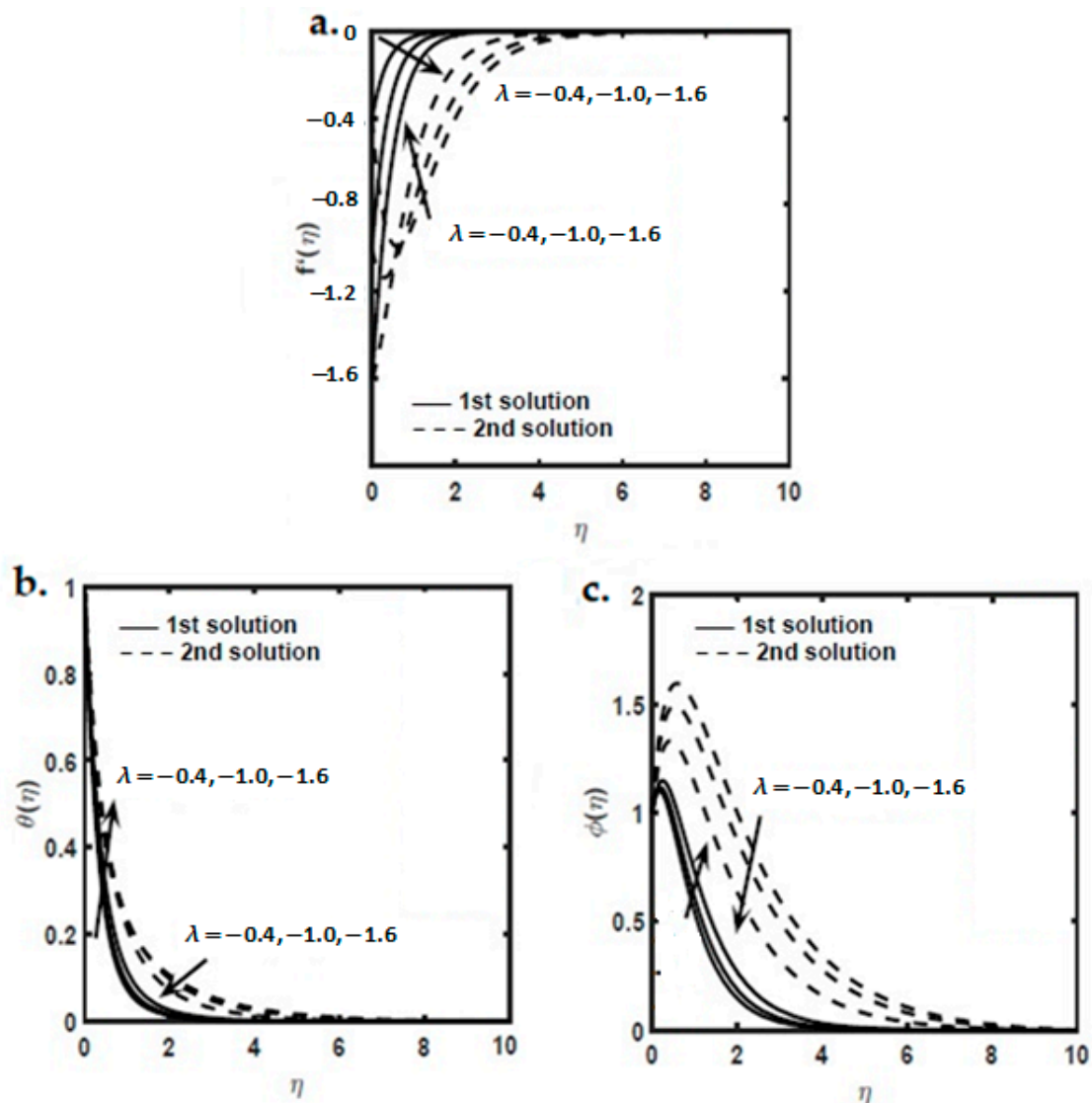


Figure 2. The impact of the shrinking parameter λ on the profiles of: (a) velocity, (b) temperature, and (c) concentration.

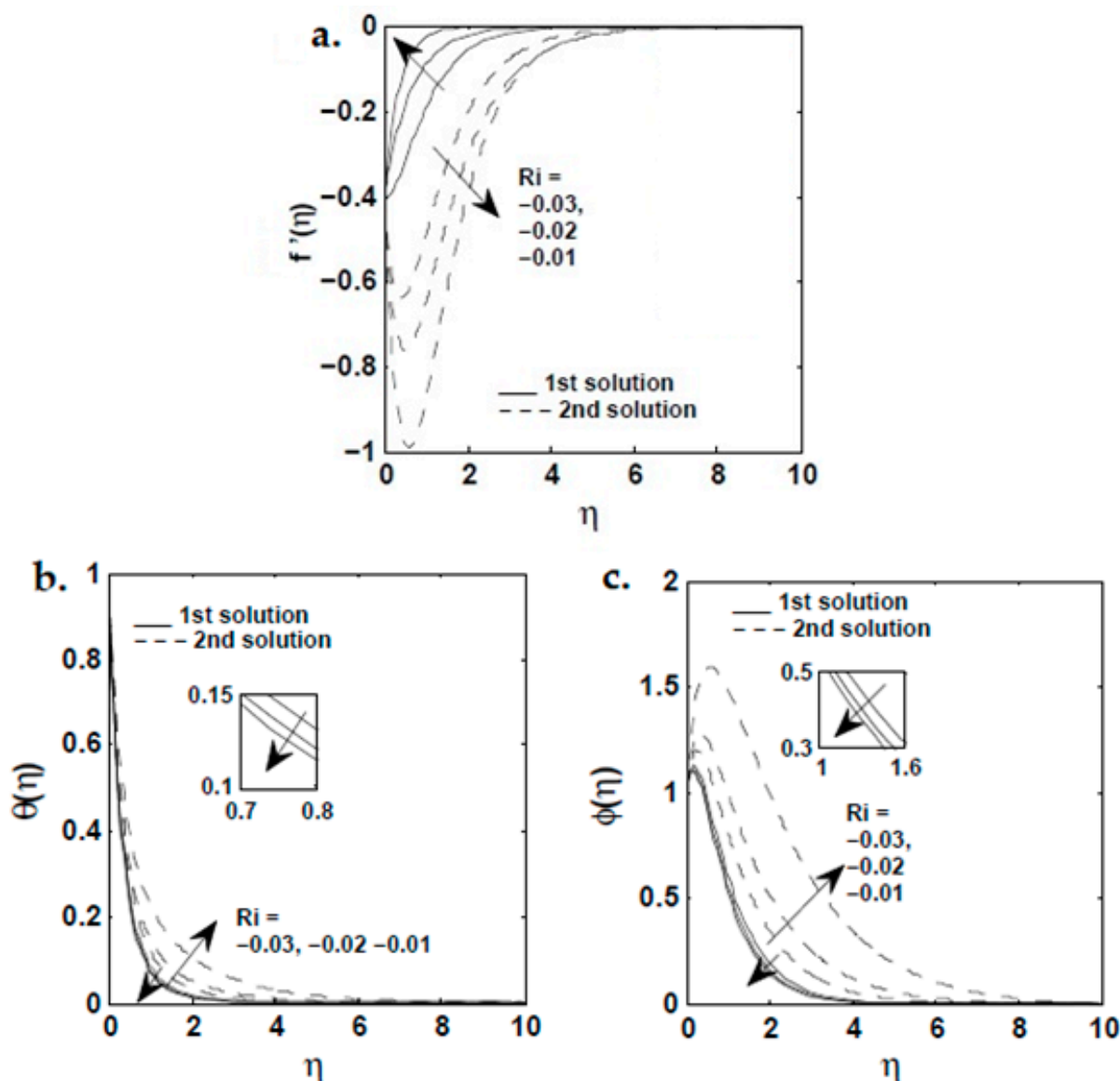


Figure 3. The impact of the opposing flow parameter for the shrinking case on the profiles of: (a) velocity, (b) temperature, and (c) concentration.

3.4. Variation in the Skin Friction Coefficient, Local Nusselt Number, and Local Sherwood Number

The distribution of the skin friction coefficient $C_f \sqrt{2Re_x} \exp(-3X/2)$, for various values of the shrinking parameter and the Soret and Dufour parameters is presented in Figure 5. The upper figure represents the first solution, and the lower figure represents the second solution. The increasing of the shrinking parameter magnitude (λ value tends to become a negative value) causes the enhancement in the skin friction coefficient in the first solution. From Figure 5, the series of $Db = 0.1$ and $Sr = 1.8$ is fixed as the reference line to compare the changes in the skin friction coefficient when the values of Sr and Db are varied. It is noticed that skin friction coefficient declines with increasing Sr and Db for the first solution. Furthermore, the skin friction coefficient rate increases with the augmentation of Db and reduction of Sr for the second solution. The graph of the skin friction coefficient $C_f \sqrt{2Re_x} \exp(-3X/2)$ against the concentration buoyancy ratio N for different values of Ri is shown in Figure 6. In this figure, the magnitude of the opposing flow rate $|Ri|$ is the main topic of discussion. It is observed that the skin friction coefficient in the first solution decreases when $|Ri|$ and N increase. The opposing flow rate in Figure 6 is denoted by $|Ri|$. The skin friction coefficient becomes smaller because the opposed buoyancy force

reduces the fluid velocity, hence the wall shear stress is also decreased. Furthermore, the skin friction coefficient in the second solution increases when Ri and N enhance.

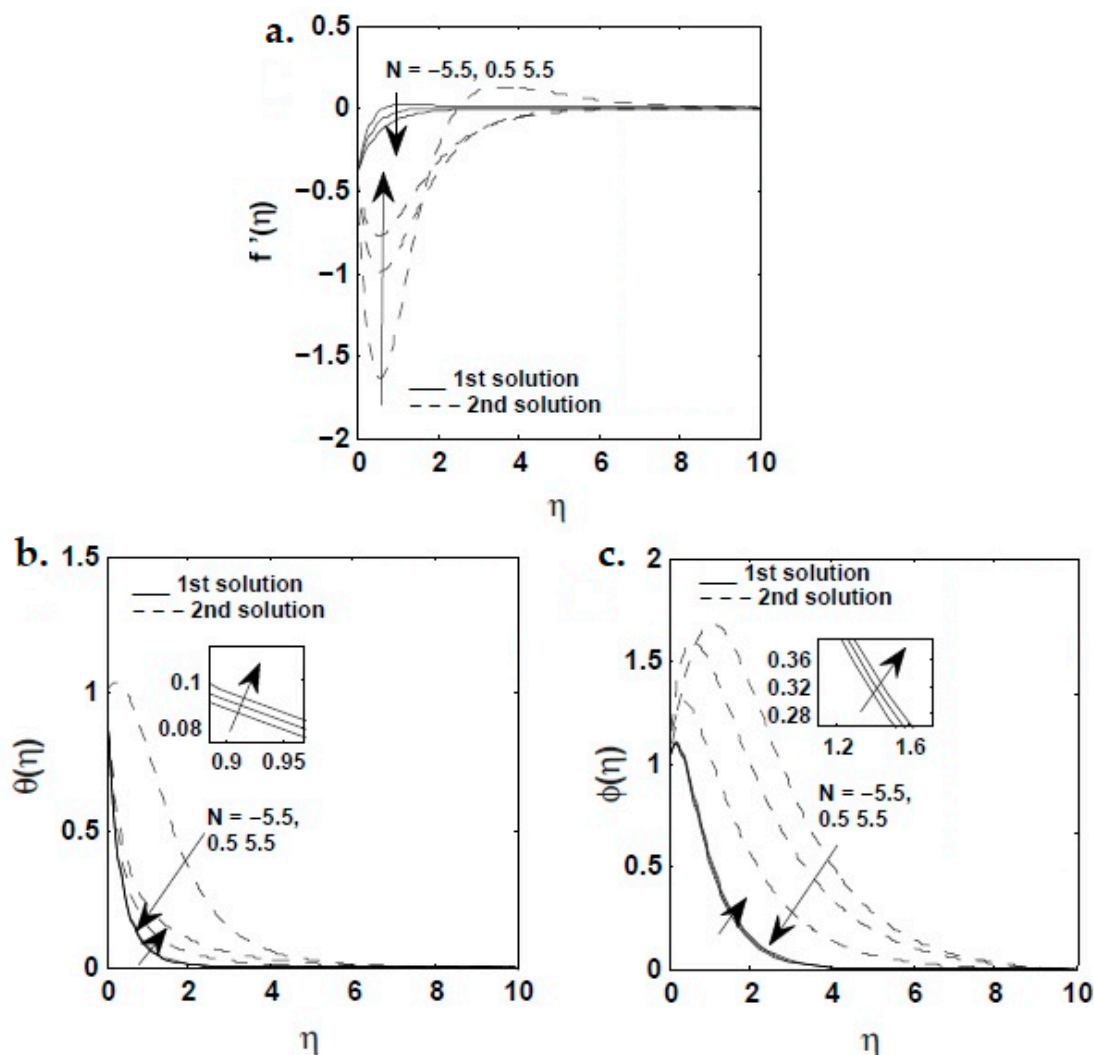


Figure 4. The impact of the buoyancy ratio parameter for the shrinking case on the profiles of: (a) velocity, (b) temperature, and (c) concentration.

Numerical graphics for the local Nusselt number $Nu_x(2/Re_x)^{1/2} \exp(-X/2)$ for different rates of the shrinking parameter and Soret and Dufour parameters are depicted in Figure 7. It is found that the shrinking parameter leads to a drop in the local Nusselt number in the first solution. However, the Soret and Dufour numbers enhance the rate of the local Nusselt number. Hence, it is proved that the heat transfer rate located at the shrinking sheet is augmented. Variations of the opposing flow rate $|Ri|$ and N on the local Nusselt number are displayed in Figure 8. It is noticed that a rise in $|Ri|$ (opposing flow rate magnitude) and in the concentration buoyancy ratio rate N result in a decrement in the local Nusselt number. An enhancement in $|Ri|$ will induce adverse pressure gradient. As a result, fluid velocity will become slow, and the wall heat transfer rate will be decreased. The graph of the local Nusselt number of the second solution against the concentration buoyancy ratio shows the existence of positive $Nu_x(2/Re_x)^{1/2} \exp(-X/2)$ at small N , and negative $Nu_x(2/Re_x)^{1/2} \exp(-X/2)$ at large N . At the positive $Nu_x(2/Re_x)^{1/2} \exp(-X/2)$ for the second solution, they are reducing for the implementation of higher opposing flow parameter. At the same time, the negative $Nu_x(2/Re_x)^{1/2} \exp(-X/2)$ in the second solution will be lowered due to the effect of $|Ri|$.

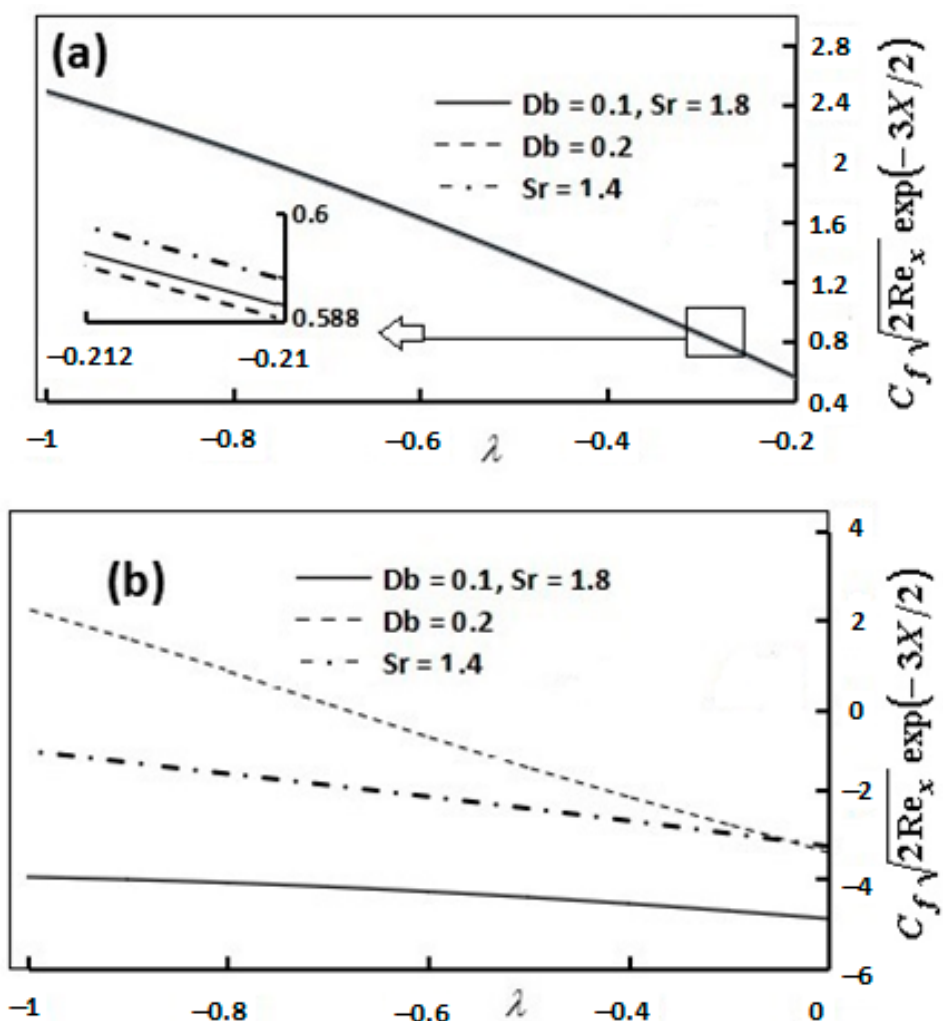


Figure 5. The variations of the skin friction coefficient $C_f \sqrt{2Re_x} \exp(-3X/2)$, against the shrinking parameter λ for various values of the Dufour and Soret number for the (a) first solution and (b) second solution.

The variation of the shrinking parameter, Soret and Dufour numbers on the local Sherwood number $Sh_x(2/Re_x)^{1/2} \exp(-X/2)$ are observed in Figures 9 and 10. The impact of the shrinking parameter is to lower the rate number of $Sh_x(2/Re_x)^{1/2} \exp(-X/2)$ in the first and second solutions, as shown in Figure 9. It is also concluded that the Soret and Dufour numbers involved in the diminution of $Sh_x(2/Re_x)^{1/2} \exp(-X/2)$ for the first solution (for all values of λ) and second solution (when the magnitude of the shrinking parameter becomes very large). Therefore, the mass transport rate is dropped at the point of the inclined exponentially shrinking sheet for the fluid flow model. Figure 10 shows that the higher rate of the concentration buoyancy ratio and opposing flow rate $|Ri|$ cause the reduction of $Sh_x(2/Re_x)^{1/2} \exp(-X/2)$ for the first solution. Because the velocity is decreased when $|Ri|$ is increased, the mass that can be transferred will be lowered (denoted by a reduced local Sherwood number). The positive and negative regions of $Sh_x(2/Re_x)^{1/2} \exp(-X/2)$ in the second solution occur at higher and lower values of N , respectively. The rising of $|Ri|$ generates a decrement in positive $Sh_x(2/Re_x)^{1/2} \exp(-X/2)$, and an increment in negative $Sh_x(2/Re_x)^{1/2} \exp(-X/2)$.

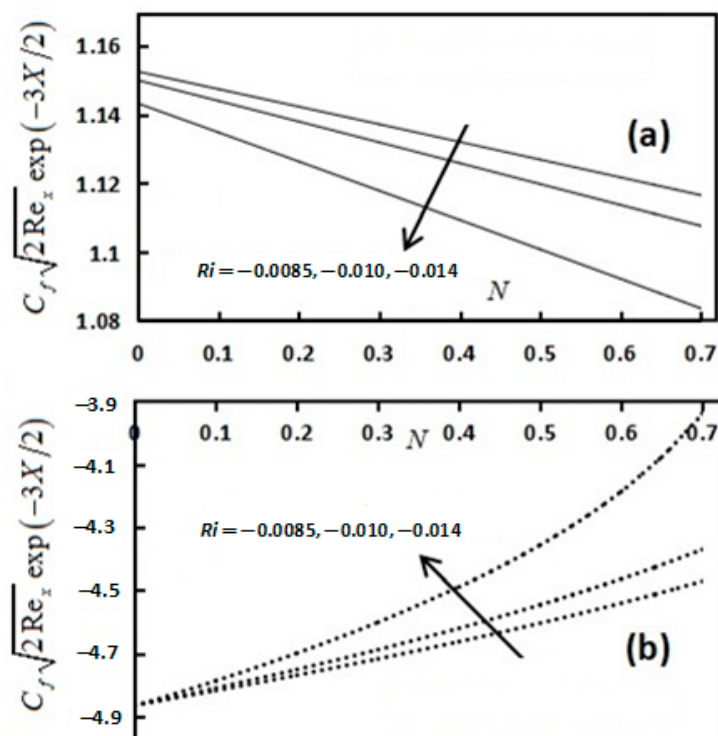


Figure 6. The impact of the buoyancy ratio parameter N on the skin friction coefficient $C_f\sqrt{2Re_x}\exp(-3X/2)$ for the various values of the opposing flow parameter Ri and when $\lambda = -0.4$ for the (a) first solution and (b) second solution.

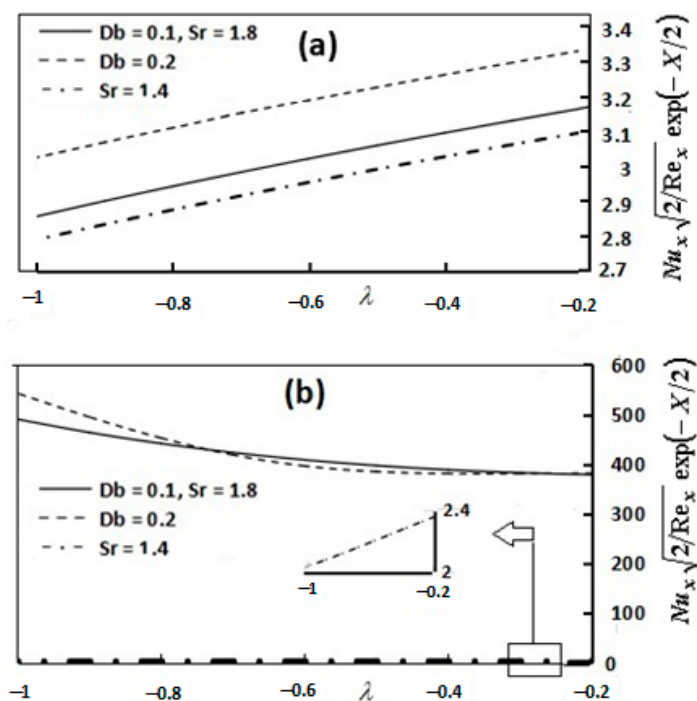


Figure 7. The variations of the local Nusselt number $Nu_x(2/Re_x)^{1/2}\exp(-X/2)$, against the shrinking parameter λ for various values of the Dufour and Soret number for the (a) first solution and (b) second solution.

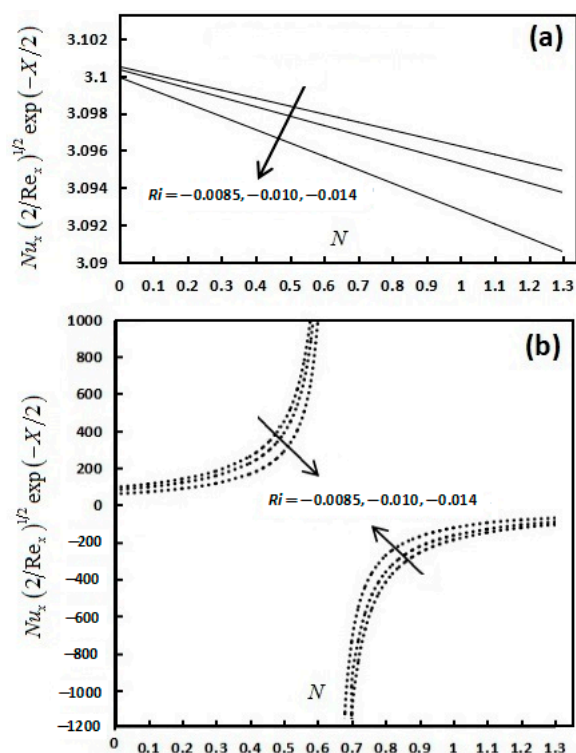


Figure 8. The impact of the buoyancy ratio parameter N on the local Nusselt number $Nu_x(2/Re_x)^{1/2} \exp(-X/2)$, for the various values of the opposing flow parameter Ri and when $\lambda = -0.4$ for the (a) first solution and (b) second solution.

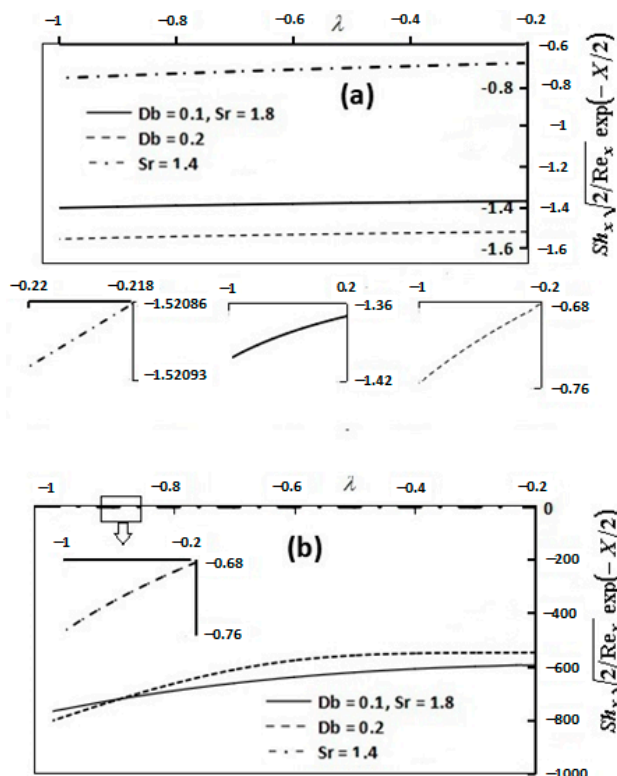


Figure 9. The variations of the local Sherwood number $Sh_x(2/Re_x)^{1/2} \exp(-X/2)$, against the shrinking parameter λ for various values of the Dufour and Soret number for the (a) first solution and (b) second solution.

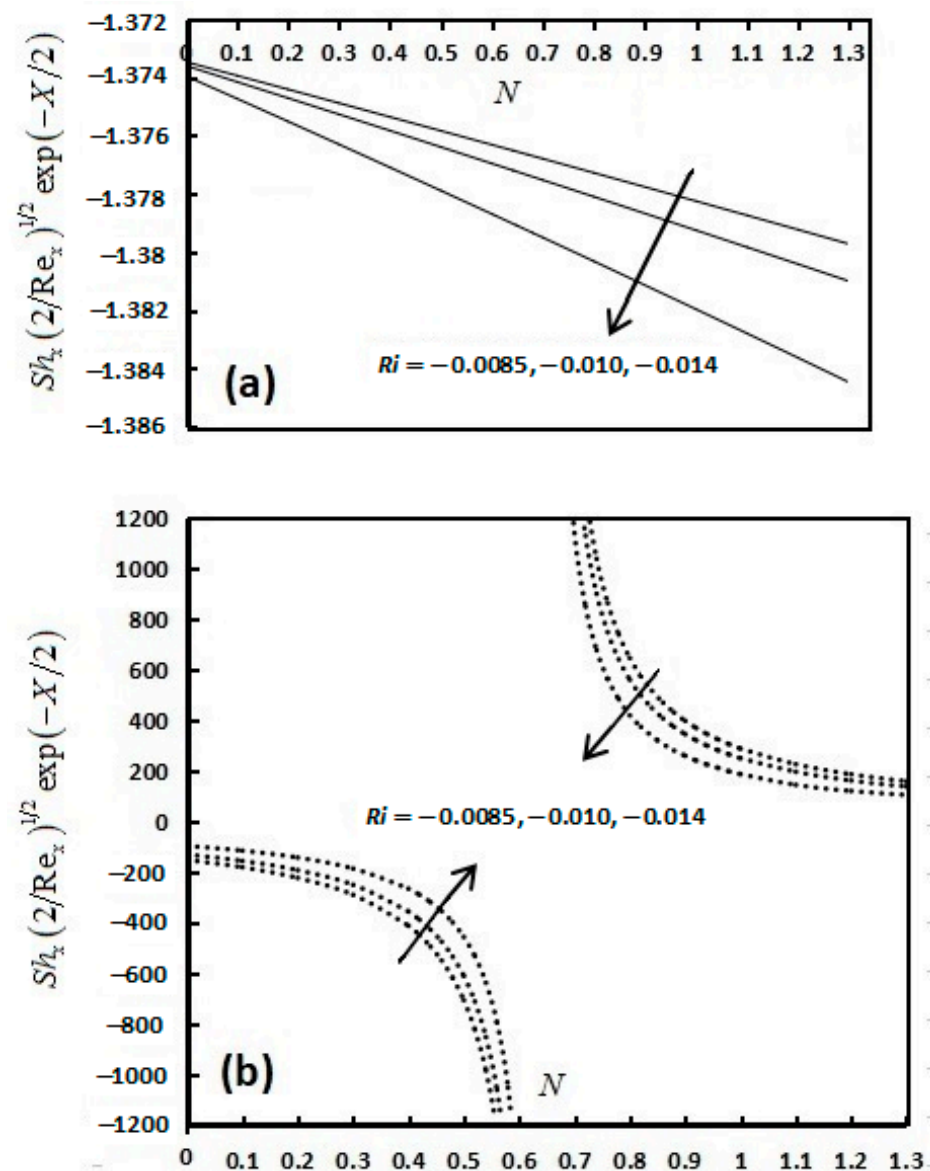


Figure 10. The impact of the buoyancy ratio parameter N on the local Sherwood number $Sh_x(2/Re_x)^{1/2} \exp(-X/2)$, for the various values of the opposing flow parameter Ri and when $\lambda = -0.4$ for the (a) first solution and (b) second solution.

4. Conclusions

The numerical results of heat and mass transfer in the boundary layer flow of Casson fluid, which is subjected to the exponential variation of an inclined shrinking sheet and when the magnetic field is projected at a certain angle, are reported in this paper. The findings are controlled by the different values of control parameters, as stated in the Results and Discussion section (Section 3). The foremost conclusions of the current numerical results, especially in the solution contributing to the actual fluid situation (first solution), are as follows:

- The impact of the shrinking parameter is to increase the temperature and concentration distributions, together with the skin friction coefficient.
- The influence of Soret and Dufour is to decrease the local Nusselt number and local Sherwood number.
- The impact of the mixed convection parameter is to enhance the instantaneous Casson fluid velocity profile and all the physical parameters.

Author Contributions: Formal analysis, S.P.; Investigation, S.P.; Methodology, S.P.; Project administration, S.S.P.M.I., N.M.A. and F.M.A.; Software, S.P.; Supervision, S.S.P.M.I., N.M.A. and F.M.A.; Validation, S.P.; Visualization, S.S.P.M.I.; Writing—original draft, F.M.A.; Writing—review & editing, S.S.P.M.I. and N.M.A. All authors have read and agreed to the published version of the manuscript.

Funding: This work was funded by Putra Grant (GP-IPM/2018/9596900) from Universiti Putra Malaysia.

Acknowledgments: The authors would like to express their gratitude to the anonymous reviewers for their valuable comments and suggestions for a betterment of this paper.

Conflicts of Interest: The authors declare no conflict of interest.

References

1. Turner, J.S. Double-diffusive phenomena. *Annu. Rev. Fluid Mech.* **1974**, *6*, 37–54. [[CrossRef](#)]
2. Schmitt, R.W. Double diffusion in oceanography. *Annu. Rev. Fluid Mech.* **1994**, *26*, 255–285. [[CrossRef](#)]
3. Huppert, H.E.; Sparks, R.S.J. Double-diffusive convection due to crystallization in magmas. *Annu. Rev. Earth Planet. Sci.* **1984**, *12*, 11–37. [[CrossRef](#)]
4. Ostrach, S. Natural convection with combined driving forces. *PhysicoChem. Hydrodyn.* **1980**, *1*, 233–247.
5. Viskanta, R.; Viskanta, R.; Bergman, T.L.; Incropera, F.P. Double-diffusive natural convection. In *Natural Convection, Fundamentals and Applications*; Kakac, S., Aung, W., Viskanta, R., Eds.; Hemisphere Pub. Corp.: Washington, DC, USA, 1985; pp. 1075–1099.
6. Bég, O.A.; Bakier, A.Y.; Prasad, V.R. Numerical study of free convection magnetohydrodynamic heat and mass transfer from a stretching surface to a saturated porous medium with Soret and Dufour effects. *Comput. Mater. Sci.* **2009**, *46*, 57–65. [[CrossRef](#)]
7. Srinivasacharya, D.; RamReddy, C. Soret and Dufour effects on mixed convection from an exponentially stretching surface. *Int. J. Nonlinear Sci.* **2011**, *12*, 60–68.
8. Sreenivasulu, P.; Reddy, N.B. Thermo-diffusion and diffusion-thermo effects on MHD boundary layer flow past an exponential stretching sheet with thermal radiation and viscous dissipation. *Adv. Appl. Sci. Res.* **2012**, *3*, 3890–3901.
9. Hayat, T.; Muhammad, T.; Shehzad, S.A.; Alsaedi, A. Soret and Dufour effects in three-dimensional flow over an exponentially stretching surface with porous medium, chemical reaction and heat source/sink. *Int. J. Numer. Method Heat Fluid Flow* **2015**, *25*, 762–781. [[CrossRef](#)]
10. Isa, S.S.P.M.; Arifin, N.M.; Farooq, U. Effect of Soret and Dufour numbers on double diffusive mixed convection boundary layer flow induced by a shrinking sheet. *J. Phys. Conf. Ser.* **2019**, *1298*, 012024. [[CrossRef](#)]
11. Azmi, H.A.; Isa, S.S.P.M.; Arifin, N.A. The boundary layer flow, heat and mass transfer beyond an exponentially stretching/shrinking inclined sheet. *CFD Lett.* **2020**, *12*, 98–107. [[CrossRef](#)]
12. Roşca, N.C.; Roşca, A.V.; Pop, I. Lie group symmetry method for MHD double-diffusive convection from a permeable vertical stretching/shrinking sheet. *Comput. Math. Appl.* **2016**, *71*, 1679–1693. [[CrossRef](#)]
13. Sharada, K.; Shankar, B. MHD mixed convection flow of a Casson fluid over an exponentially stretching surface with the effects of soret, dufour, thermal radiation and chemical reaction. *WJM* **2015**, *5*, 165. [[CrossRef](#)]
14. Gireesha, B.J.; Archana, M.; Prasannakumara, B.C.; Gorla, R.S.R.; Makinde, O.D. MHD three dimensional double diffusive flow of Casson nanofluid with buoyancy forces and nonlinear thermal radiation over a stretching surface. *Int. J. Numer. Methods Heat Fluid Flow* **2017**, *27*, 2858–2878. [[CrossRef](#)]
15. Kumar, K.G.; Ramesh, G.K.; Gireesha, B.J. Numerical solutions of double-diffusive natural convection flow of MHD Casson fluid over a stretching vertical surface with thermal radiation. *JNAAM* **2017**, *2*, 6–14.
16. Pal, D.; Roy, N. Lie group transformation on MHD double-diffusion convection of a Casson nanofluid over a vertical stretching/shrinking surface with thermal radiation and chemical reaction. *Int. J. Appl. Comput. Math.* **2018**, *4*, 13. [[CrossRef](#)]
17. Ullah, I.; Khan, I.; Shafie, S. Soret and Dufour effects on unsteady mixed convection slip flow of Casson fluid over a nonlinearly stretching sheet with convective boundary condition. *Sci. Rep.* **2017**, *7*, 1–19. [[CrossRef](#)]
18. Das, M.; Mahanta, G.; Shaw, S.; Parida, S.B. Unsteady MHD chemically reactive double-diffusive Casson fluid past a flat plate in porous medium with heat and mass transfer. *Heat Transf. Asian Res.* **2019**, *48*, 1761–1777. [[CrossRef](#)]
19. Prasad, D.V.K.; Chaitanya, G.S.K.; Raju, R.S. Double diffusive effects on mixed convection Casson fluid flow past a wavy inclined plate in presence of Darcian porous medium. *Results Eng.* **2019**, *3*, 100019. [[CrossRef](#)]
20. Manjappa, A.; Jayanna, G.B.; Chandrappa, P.B. Triple diffusive flow of Casson nanofluid with buoyancy forces and nonlinear thermal radiation over a horizontal plate. *Arch. Thermodyn.* **2019**, *40*, 49–69. [[CrossRef](#)]
21. Alizadeh, R.; Gomari, S.R.; Alizadeh, A.; Karimi, N.; Li, L.K.B. Combined heat and mass transfer and thermodynamic irreversibilities in the stagnation-point flow of Casson rheological fluid over a cylinder with catalytic reactions and inside a porous medium under local thermal nonequilibrium. *Comput. Math. Appl.* **2019**, *81*, 786–810. [[CrossRef](#)]
22. Rafique, K.; Anwar, M.I.; Misiran, M.; Khan, I.; Alharbi, S.O.; Thounthong, P.; Nisar, K.S. Keller-box analysis of Buongiorno model with Brownian and thermophoretic diffusion for Casson nanofluid over an inclined surface. *Symmetry* **2019**, *11*, 1370. [[CrossRef](#)]
23. Lund, L.A.; Omar, Z.; Raza, J.; Khan, I.; Sherif, E.M. Effects of Stefan blowing and slip conditions on unsteady MHD Casson nanofluid flow over an unsteady shrinking sheet: Dual solutions. *Symmetry* **2020**, *12*, 487. [[CrossRef](#)]

24. Lund, L.A.; Omar, Z.; Khan, I.; Baleanu, D.; Nisar, K.S. Convective effect on magnetohydrodynamic (MHD) stagnation point flow of Casson fluid over a vertical exponentially stretching/shrinking surface: Triple solutions. *Symmetry* **2020**, *12*, 1238. [[CrossRef](#)]
25. Bhattacharyya, K.; Layek, G.C.; Seth, G.S. Soret and Dufour effects on convective heat and mass transfer in stagnation-point flow towards a shrinking surface. *Phys. Scr.* **2014**, *89*, 095203. [[CrossRef](#)]
26. Khan, N.A.; Sultan, F. On the double diffusive convection flow of Eyring-Powell fluid due to cone through a porous medium with Soret and Dufour effects. *AIP Adv.* **2015**, *5*, 057140. [[CrossRef](#)]
27. Kefayati, G. Soret and Dufour effects on double diffusive mixed convection of Newtonian and shear-thinning fluids in a two sided lid-driven cavity. *Eng. Comput.* **2016**, *33*, 2117–2148. [[CrossRef](#)]
28. Lagra, A.; Bourich, M.; Hasnaoui, M.; Amahmid, A.; Er-Raki, M. Analytical and Numerical Study of Soret and Dufour Effects on Double Diffusive Convection in a Shallow Horizontal Binary Fluid Layer Submitted to Uniform Fluxes of Heat and Mass. *Math. Probl. Eng.* **2018**, *2018*, 7946078. [[CrossRef](#)]
29. Kasmani, R.M.; Sivasankaran, S.; Bhuvanewari, M.; Alshomrani, A.S.; Siri, Z. Soret and Dufour effects on doubly diffusive convection of nanofluid over a wedge in the presence of thermal radiation and suction. *Sci. Iran. B* **2019**, *26*, 2817–2826. [[CrossRef](#)]
30. Dzulkifli, N.F.; Bachok, N.; Pop, I.; Yacob, N.A.; Arifin, N.M.; Rosali, H. Stability of Partial slip, Soret and Dufour effects on unsteady boundary layer flow and heat transfer in Copper-water nanofluid over a stretching/shrinking sheet. *J. Phys. Conf. Ser.* **2017**, *890*, 012031. [[CrossRef](#)]
31. Dzulkifli, N.F.; Bachok, N.; Pop, I.; Yacob, N.A.; Arifin, N.M.; Rosali, H. Soret and Dufour effects on unsteady boundary layer flow and heat transfer of nanofluid over a stretching/shrinking sheet: A stability analysis. *J. Chem. Eng. Process Technol.* **2017**, *8*, 1000336. [[CrossRef](#)]
32. Najib, N.; Bachok, N.; Arifin, N.M.; Ali, F.M. Stability analysis of stagnation-point flow in a nanofluid over a stretching/shrinking sheet with second-order slip, soret and dufour effects: A revised model. *Appl. Sci.* **2018**, *8*, 642. [[CrossRef](#)]
33. Hayat, T.; Shafiq, A.; Alsaedi, A.; Asghar, S. Effect of inclined magnetic field in flow of third grade fluid with variable thermal conductivity. *AIP Adv.* **2015**, *5*, 087108. [[CrossRef](#)]
34. Weidman, P.D.; Kubitschek, D.G.; Davis, A.M.J. The effect of transpiration on self-similar boundary layer flow over moving surfaces. *Int. J. Eng. Sci.* **2006**, *44*, 730–737. [[CrossRef](#)]
35. Harris, S.D.; Ingham, D.B.; Pop, I. Mixed convection boundary-layer flow near the stagnation point on a vertical surface in a porous medium: Brinkman model with slip. *Transp. Porous Media* **2009**, *77*, 267–285. [[CrossRef](#)]
36. Magyari, E.; Keller, B. Heat and mass transfer in the boundary layers on an exponentially stretching continuous surface. *J. Phys. D Appl. Phys.* **1999**, *32*, 577. [[CrossRef](#)]
37. Yasin, M.H.M.; Ishak, A.; Pop, I. MHD stagnation-point flow and heat transfer with effects of viscous dissipation, Joule heating and partial velocity slip. *Sci. Rep.* **2015**, *5*, 17848. [[CrossRef](#)]
38. Abbas, Z.; Sheikh, M.; Pop, I. Stagnation-point flow of a hydromagnetic viscous fluid over stretching/shrinking sheet with generalized slip condition in the presence of homogeneous–heterogeneous reactions. *J. Taiwan Inst. Chem. Eng.* **2015**, *55*, 69–75. [[CrossRef](#)]
39. Yahaya, R.I.; Arifin, N.M.; Isa, S.S.P.M. Stability analysis on magnetohydrodynamic flow of casson fluid over a shrinking sheet with homogeneous-heterogeneous reactions. *Entropy* **2018**, *20*, 652. [[CrossRef](#)]